Surfaces and Interfaces 46 (2024) 104055

Contents lists available at ScienceDirect

Surfaces and Interfaces

journal homepage: www.sciencedirect.com/journal/surfaces-and-interfaces

3D lattice Boltzmann simulation of self-propelled single-droplet jumping on microstructured surfaces during condensation

Yuhao Zhu [a], Shan Gao [b,c], Zhichun Liu [a,*], Wei Liu [a]

[a] School of Energy and Power Engineering, Huazhong University of Science and Technology (HUST), Wuhan 430074, China
[b] School of Energy and Power Engineering, Jiangsu University, Zhenjiang 212013, China
[c] Key Laboratory for Thermal Science and Power Engineering of Ministry of Education, Department of Engineering Mechanics, Tsinghua University, Beijing 100084, China

ARTICLE INFO

Keywords:
Self-propelled droplet transport
Directional single-droplet jumping
Laplace pressure difference
Microstructured surface

ABSTRACT

Self-propelled droplet transport on surfaces can re-expose the condensation nucleation sites and is crucial for the enhancement of dropwise condensation heat transfer. In this paper, dropwise condensation and Laplace pressure driven single-droplet jumping on microstructured surfaces are simulated by a three-dimensional non-orthogonal MRT pseudopotential lattice Boltzmann model. The overall process of dropwise condensation on micropillar surfaces, including dewetting transitions and single droplet jumping, is well observed. The simulation results indicate that there is an optimal aspect ratio for the droplet to reach maximum detaching velocity. The energy conversion efficiency from surface energy to kinetic energy reaches ~14.2 % when the aspect ratio equals 3.0. Moreover, the effect of microstructure on droplet directional jumping is analyzed. It is demonstrated that the droplet's movement relies on both the direction of the micropillars and the expansion direction of the top liquid sphere due to the pressing effect of the liquid column. To control the jumping direction of the droplet, it is essential to utilize microstructures to regulate the bursting phase of the droplet. Our study illustrates the mechanism of single droplet jumping during condensation and provides guidance for the design of surface structures for the directional transport of condensed droplets.

1. Introduction

The transition of droplet wetting states during condensation and spontaneous transport on a surface is critical for applications including water collection [1,2], microfluidic systems [3], anti-icing [4], and phase-change heat transfer [5]. In order to trigger the detachment of droplets and realize liquid vapor separation, the introduction of an external force field is a convenient and effective method, including gravity and electric field [6–9]. In recent years, Laplace pressure difference within a deformed droplet induced by surface structures has been identified as one of the main driving forces for self-propelled droplet transport [10,11]. The main factors affecting droplet transport include surface chemistry and structural properties, such as wetting behavior and hierarchical structure [12–14]. The existence of Laplace pressure provides the possibility for the spontaneous transition of droplets from Wenzel state to Cassie state during condensation [15]. In addition, Laplace pressure driven single-droplet jumping from microgrooves is also observed, which is triggered by the overflow or depinning of the deformed droplet [16,17]. It is proposed that up to 50–60 % energy conversion efficiency of droplet self-jumping can be achieved by the rational design of microgrooves [10]. Researchers have observed that the maximum jump velocity of a single droplet can reach ~0.5 m/s [10], which makes the application of the phenomenon to condensate reflux in heat pipes possible. For ultra-thin vapor chambers (UTVCs), when the thickness of the cavity is less than 0.3 mm, the thermal resistance of UTVC will increase sharply due to the reduction of the capillary transport capacity [18]. The single droplet jumping mode can provide an additional means of reflux for the UTVCs, and the microstructure occupies less space in the vapor cavity, thus alleviating the increase in vapor diffusion resistance. In addition, with the emergence of microstructures that can respond to changes in the magnetic field [19], the direction of single droplet jumping becomes adjustable, which makes it highly valuable for applications in microfluidics and self-cleaning during phase changes. Therefore, it is of great significance to quantify and analyze the phenomenon of single-droplet jumping on common structures, and further to study the influence of the structure on

* Corresponding author at: School of Energy and Power Engineering, Huazhong University of Science and Technology (HUST), Wuhan 430074, China.
E-mail address: zcliu@hust.edu.cn (Z. Liu).

https://doi.org/10.1016/j.surfin.2024.104055
Received 11 September 2023; Received in revised form 27 January 2024; Accepted 7 February 2024
Available online 14 February 2024

the direction of spontaneous droplet transport.

In terms of numerical computation, traditional CFD simulations have been mainly focused on film condensation and internal flow condensation [20]. Recently, lattice Boltzmann method (LBM) as a mesoscopic method has been comprehensively applied to simulating multiphase flows and phase change heat transfer problems [21–23]. The pseudo-potential LB method proposed by Shan and Chen has achieved great success in simulating multiphase problems due to its simplicity and efficiency [24]. Afterward, Mukherjee and Abraham proposed a multiple-relaxation-time (MRT) multiphase LB model, which possesses higher numerical stability and can be applied to high-density-ratio problems [25]. In order to solve the temperature field, a double-distribution-function (DDF) approach has been devised, utilizing a temperature distribution function to calculate the energy equation [26]. On the other hand, a hybrid thermal LB method is also proposed, in which the finite-difference method is directly applied to calculate the temperature field [27]. By employing these two methods, dropwise condensation on microstructured surfaces can therefore be simulated [21]. In recent years, numerical investigations have begun to focus on hydrodynamics during dropwise condensation, including the effects of surface wettability, subcooling degree and morphologies [21,28-30]. By tuning surface wettability, it is found that wetting state changes from Wenzel state to Cassie state with the increase of surface hydrophobicity [28]. These results show that LB method can easily capture the whole process of condensation from droplet nucleation to jumping and show the local heat transfer performance. In recent years, a lot of the studies on self-propelled droplet transport are focused on coalescence-induced jumping of two droplets [8,31-33]. Single-droplet jumping induced by Laplace pressure difference possesses ultrahigh surface-energy-to-kinetic-energy conversion efficiency, but the corresponding numerical analysis is still lacking. Besides, wetting state transition and directional jumping induced by Laplace pressure difference are rarely studied and quantified by numerical simulations [34].

In this paper, the triggering conditions for single-droplet jumping and the energy conversion efficiency are calculated and analyzed. Considering the possible applications in the field of self-cleaning, the paper further simulates the directional jumping of single droplets, and comparatively analyzes the ability of directional jumping of droplets under different structures. The research work provides certain theoretical guidance for the application of microstructured superhydrophobic surfaces in the field of liquid reflux and microfluidics.

2. Numerical method

In this work, a three-dimensional non-orthogonal MRT-LB model [35] is applied to simulate wetting state transition and single-droplet jumping during condensation on micro-pillar structured surfaces. D3Q19 lattice model is chosen to describe discrete velocities [36]. The interaction force term proposed by Gong and Cheng is adopted, incorporating the Peng–Robinson (P–R) equation of state (EOS) in the interaction potential [37].

The MRT density distribution equation can be written as

$$f_i(\mathbf{x}+\mathbf{e}_i\delta_t, t+\delta_t) = f_i(\mathbf{x},t) - \Lambda_{ij}\left(f_j - f_j^{eq}\right)\big|_{(\mathbf{x},t)} + \frac{\delta_t}{2}\left[G_i\big|_{(\mathbf{x}+\mathbf{e}_i\delta_t, t+\delta_t)} + G_i\big|_{(\mathbf{x},t)}\right] \tag{1}$$

where $f_i(\mathbf{x},t)$ is the density distribution function at the spatial position $\mathbf{x}$ and time t, $f_i^{eq}(\mathbf{x},t)$ is the corresponding equilibrium distribution function, $\mathbf{e}_i$ is the discrete speed in i th direction, the collision operator Λ_{ij} is given by $\Lambda_{ij} = (\mathbf{M}^{-1}\mathbf{\Lambda}\mathbf{M})_{ij}$ in which $\mathbf{M}$ is the orthogonal transformation matrix and $\mathbf{\Lambda}$ is a diagonal matrix, and G_i is the forcing term [35]. By linear transformation, $\mathbf{f}$ and $\mathbf{f}^{eq}$ can be projected onto the moment space with $\mathbf{m} = \mathbf{M}\mathbf{f}$ and $\mathbf{m}^{eq} = \mathbf{M}\mathbf{f}^{eq}$. Then the collision process can be written as

$$\mathbf{m}^* = \mathbf{m} - \mathbf{\Lambda}(\mathbf{m} - \mathbf{m}^{eq}) + \delta_t\left(\mathbf{I} - \frac{\mathbf{\Lambda}}{2}\right)\mathbf{S} \tag{2}$$

where $\mathbf{S}$ is the forcing term in the moment space and $\mathbf{I}$ is the unit matrix. The diagonal matrix $\mathbf{\Lambda}$ is given as

$$\mathbf{\Lambda} = \mathrm{diag}(1,1,1,1,s_e,s_\nu,s_\nu,s_\nu,s_\nu,s_\nu,s_q,s_q,s_q,s_q,s_q,s_q,s_\pi,s_\pi,s_\pi) \tag{3}$$

whose elements represent the inverse of the relaxation time. In this study, the parameters are chosen as $s_e = 0.8$, $s_q = s_\pi = 1.0$ and s_ν is chosen as $s_\nu^{-1} = 0.68$, which is equivalent to the kinetic viscosity $\nu = 0.06$. Then through streaming process, the density distribution function in the velocity space can be obtained and the macroscopic density and momentum can be calculated by

$$\rho = \sum_i f_i, \rho\mathbf{u} = \sum_i \mathbf{e}_i f_i + \frac{\delta_t}{2}\mathbf{F} \tag{4}$$

The total force applied to the system $\mathbf{F}$ is given by

$$\mathbf{F} = \mathbf{F}_{int} + \mathbf{F}_g + \mathbf{F}_s \tag{5}$$

where $\mathbf{F}_{int}$ is the fluid-fluid interaction force term, $\mathbf{F}_g$ is the gravitational force and $\mathbf{F}_s$ is the fluid-solid interaction force. In this work, the fluid-fluid interaction force term proposed by Gong and Cheng is adopted, which is given as [37]

$$\mathbf{F}_{int} = -\beta\psi(\mathbf{x})\sum_i G(\mathbf{x}+\mathbf{e}_i\delta_t)\psi(\mathbf{x}+\mathbf{e}_i\delta_t)\mathbf{e}_i - \frac{1-\beta}{2}\sum_i G(\mathbf{x}+\mathbf{e}_i\delta_t)\psi^2(\mathbf{x}+\mathbf{e}_i\delta_t)\mathbf{e}_i \tag{6}$$

where β is the weighting factor depending on the equation of state, $G(\boldsymbol{x}+\mathbf{e}_i)$ indicates the interaction strength. For D3Q19 model, $G_{1-6} = 1/6$ and $G_{7-18} = 1/12$. The interaction potential $\psi(\mathbf{x})$ can be written as

$$\psi(\mathbf{x}) = \sqrt{\frac{2\left(p_{EOS} - \rho c_s^2\right)}{Gc^2}} \tag{7}$$

where p_{EOS} can be solved from the equation of state, c_s is the lattice sound speed and $c = 1$ is the lattice constant [38]. In this work, P–R equation of state is chosen, which is proved a more accurate EOS for water and ammonia [37]

$$p = \frac{\rho RT}{1-b\rho} - \frac{a\rho^2\alpha(T)}{1+2b\rho-b^2\rho^2} \tag{8}$$

where $\alpha(T) = [1 + (0.37464 + 1.54226\omega - 0.26992\omega^2)(1 - \sqrt{T/T_c})^2]$ and ω is the acentric factor which equals to 0.344 for water.

The fluid-solid interaction force $\mathbf{F}_s$ is given as [37]

$$\mathbf{F}_s = -\psi(\mathbf{x})\sum_i G_s\omega_i s(\mathbf{x}+\mathbf{e}_i\delta_t)\mathbf{e}_i\delta_t \tag{9}$$

where G_s indicates the solid-fluid interaction strength, ω_i is the weighting coefficient and $s(\mathbf{x})$ is the indicator function which is equal to 1 for solid and 0 for fluid. For D3Q19, the coefficient $\omega_i = 1/3$ ($i = 0$), $\omega_i = 1/18$ ($i = 1$–6) and $\omega_i = 1/36$ ($i = 7$–18). The gravitational force is given by

$$\mathbf{F}_g = g\cdot(\rho(\mathbf{x}) - \rho_{ave}) \tag{10}$$

where g is gravitational acceleration and ρ_{ave} is the average density of the computational domain.

The energy equation model proposed by Gong and Cheng is applied [39]. Through neglecting the viscous heat dissipation, the temperature equation is given by [40]

$$\rho c_v\frac{DT}{Dt} = \nabla\cdot(\lambda\nabla T) - T\left(\frac{\partial p_{EOS}}{\partial T}\right)_\rho \nabla\cdot\mathbf{u} \tag{11}$$

where c_v is the specific heat at constant volume and λ is the thermal conductivity. It should be noted that the physical parameters at the vapor-liquid interface (such as kinematic viscosity, specific heat and thermal diffusivity) can be calculated as

$$\chi = \chi_{\text{liquid}} \cdot \frac{\rho - \rho_{\text{vapor}}}{\rho_{\text{liquid}} - \rho_{\text{vapor}}} + \chi_{\text{vapor}} \cdot \frac{\rho_{\text{liquid}} - \rho}{\rho_{\text{liquid}} - \rho_{\text{vapor}}} \tag{12}$$

The computations are performed on an Intel(R) Core(TM) i5–8400 processor with 2.80 GHz speed and 16GB RAM. The code is written in Fortran and compiled with GFortran.

3. Model validation

Two tests are conducted to validate the three-dimensional MRT-LB model. First, the Laplace law is checked to verify the hydrodynamic effects of the model. Then, D^2 law is also examined by recording the droplet diameter change during evaporation to verify the phase change process.

According to the Laplace law, the capillary pressure for 3D simulation satisfies the following equation

$$\Delta p = 2\sigma / r \tag{13}$$

where Δp represents the pressure difference inside and outside the droplet, σ is the surface tension and r is the droplet radius. To calculate the pressure difference, a droplet is set in the center of a 100 × 100 × 100 lattice units domain filled with saturated vapor. The calculation ignores gravity with periodic boundary conditions applied all around. By adjusting the droplet radius, the variation of Δp with r is shown in Fig. 1(a), where Δp is proportional to $1/r$ and the slope of the fitted line $\sigma = 0.07$. Moreover, the relationship between surface tension and saturated temperature for droplets is shown in Fig. 1(b), where the surface tension decreases linearly with the increase of saturation temperature. It can be seen that the calculation results agree well with the Laplace law.

Secondly, phase change process of the model, including droplet evaporation and condensation, is verified. D^2 law is considered to verify the evaporation process. The setup of the calculation domain is basically the same as above with droplet radius $r = 30$ lattice units. The temperature of the droplet is initialized to $0.82T_c$ and the droplet is in saturated state. The temperature of saturated vapor is set to $0.86T_c$ and $0.88T_c$. As shown in Fig. 2, the square of the droplet diameter decreases linearly with time which is in good agreement with D^2 law. On the other hand, simulations of single droplet condensation growth are used to validate the condensation process. For a three-dimensional single-droplet condensation process, the droplet radius versus time should satisfy the power law ($r \sim t^a$), with the power law exponent $0.23 \le a \le 0.5$, suggested by experimental and theoretical studies [41,42]. Constant temperature $T_w = 0.6T_c$ is applied at the bottom center to simulate single droplet condensation process. As shown in Fig. 2(b), when the saturated vapor temperature is set to $0.9T_c$ and $0.95T_c$, the power law exponent $a = 0.24$ and $a = 0.34$. The difference between our numerical values and theoretical results is within the normal range of previous theoretical and experimental studies [41]. Therefore, this model is reliable for the simulations of dropwise condensation.

4. Results and discussion

4.1. Boundary conditions and parameter settings

The computational domain is chosen as 70 × 70 × 140 lattices. The basic structure of the simulation is a configuration of four vertical micropillars shown in Fig. 3(a). The halfway bounce-back scheme is applied at the solid surface to deal with no-slip boundary condition [43] and constant temperature $T_w = 0.6T_c$ at the bottom. The intrinsic contact angle of the surface is set as $\theta_w = 160°$. Pressure boundary condition is employed at the top of the domain with saturated vapor temperature $T_s = 0.82T_c$ [44]. And periodic boundary is used for the remaining perimeter.

To convert lattice units to physical units, capillary length is often chosen as the characteristic length of the condensation process [21,36].

$$l_0 = \sqrt{\frac{\sigma}{g(\rho_l - \rho_v)}}, u_0 = \sqrt{g l_0}, t_0 = l_0 \Big/ u_0 \tag{14}$$

where l_0 is the capillary length, ρ_l and ρ_v are the density of saturated water and vapor, u_0 is the characteristic velocity, g is the gravitational acceleration and t_0 is the characteristic time. Then, the relationship between lattice units and physical units can be calculated: $l^{\text{real}}/l^{\text{lu}} = l_0^{\text{real}}/l_0^{\text{lu}}$, $t^{\text{real}}/t^{\text{lu}} = t_0^{\text{real}}/t_0^{\text{lu}}$. In this study, the gravitational acceleration in the numerical simulation is set to 1.5×10^{-8}. The coexistence densities at saturated temperature $T_s = 0.82T_c$ are $\rho_l = 6.98$ and $\rho_v = 0.25$ with density ratio $\rho_l/\rho_v = 27.9$. By corresponding to the actual temperature and density ratio, it is drawn that $l_0^{\text{real}}/l_0^{\text{lu}} = 2$ μm/lu and $t_0^{\text{real}}/t_0^{\text{lu}} = 5.6 \times 10^{-5}$ ms/ts. Other physical parameters are set as follows: specific heat capacity $c_{p,l} = c_{v,l} = 4.0$, $c_{p,v} = c_{v,v} = 2.0$; dynamic viscosity $\mu_l = 0.4187$, $\mu_v = 0.0149$; thermal diffusivity $a_l = 0.07$, $a_v = 0.04$. Therefore, the Prandtl number can be derived: $Pr_l = 0.86$, $Pr_v = 1.5$.

The degree of subcooling is characterized by the Jacob number:

$$Ja = \frac{c_{p,v}(T_w - T_s)}{h_{fg}} = \frac{c_{p,v} \cdot \Delta T}{h_{fg}} \tag{15}$$

where T_w is the wall temperature, T_s represents the saturation temperature and $h_{fg} = 0.21$ is the latent heat which can be obtained by the latent heat calculation method [45]. For saturated vapor temperature T_s

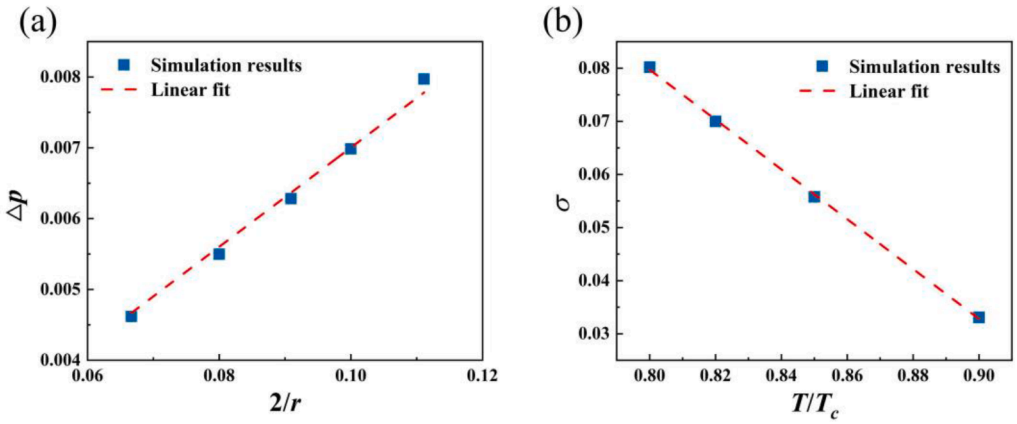

Fig. 1. Verification of Laplace law. (a) Variation of the pressure difference Δp with droplet radius r; (b) Relationship between surface tension and saturated temperature (T_c represents the critical temperature).

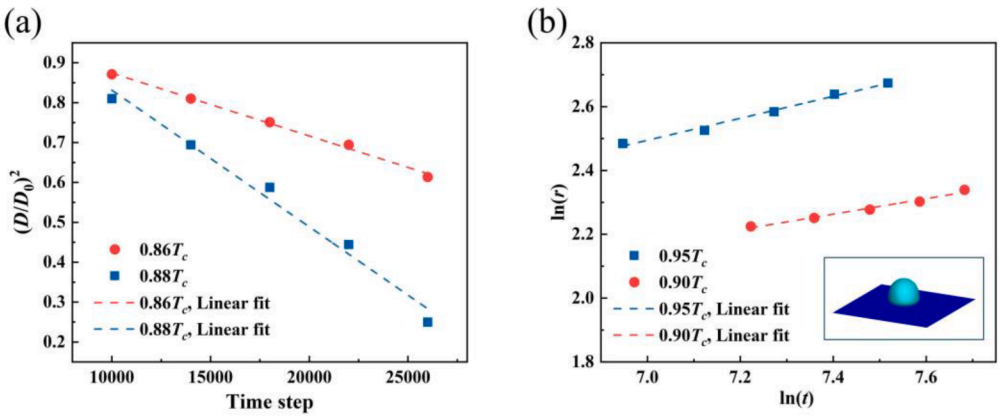

Fig. 2. Verifications of phase change process. (a) evaporation simulation for D^2 law; (b) condensation simulation for power law.

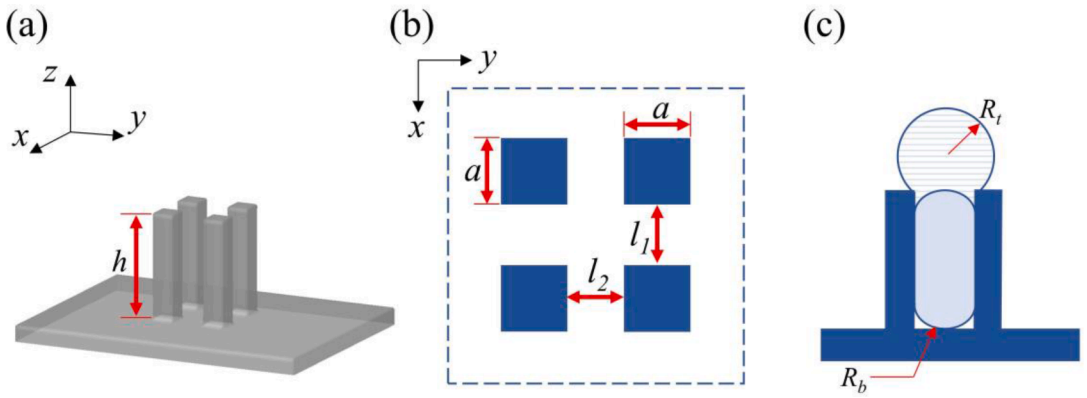

Fig. 3. Schematic diagram of the microstructure. (a) Structured surface with micropillars (pillar height h, saturated vapor temperature $T_s = 0.82T_c$ and surface temperature $T_w = 0.6T_c$); (b) Top view schematic of the simulated surface with width of micropillar a, spacing l_1 and l_2; (c) Schematic diagram of droplet condensation, where R_t is the radius of curvature of the top and R_b represents the radius of curvature of the bottom.

$= 0.82T_c$ and surface temperature $T_w = 0.6T_c$, the Jacob number $Ja =$ 0.076.

4.2. Single droplet jumping phenomenon during condensation

The evolution of the condensate droplet with time for surface parameters $h = 56\mu m$, $l_1 = l_2 = 16\mu m$ and $a = 12\mu m$ is shown in Fig. 4. The intrinsic contact angle is set as $\theta = 160°$. It can be seen that the nucleation and growth of the condensate droplet is confined between the microcolumns until the top of the droplet exceeds the microstructure and eventually single-droplet jumping occurs. As shown in Fig. 3(c), Laplace pressure difference of the deformed droplet can be written as $\Delta p_L \approx 2\sigma(1/r_b\text{-}1/r_t)$, where R_t represents the radius of curvature of the top and R_b represents the radius of curvature of the bottom. The unrestricted growth of the top of the droplet leads to an increasing Laplace pressure difference, which eventually causes the dewetting phenomenon and subsequent single-droplet jumping.

In order to further monitor the condensation process, the height of center of mass is calculated through

$$H(t) = \frac{\sum m(\mathbf{x},t)h(\mathbf{x},t)}{\sum m(\mathbf{x},t)} \tag{16}$$

where $H(t)$ represents the height of the center of mass of the droplet, $m(\mathbf{x},t)$ is the local mass and $h(\mathbf{x},t)$ is the corresponding local height. And the instantaneous ascending velocity during condensation can be obtained by deriving $H(t)$. The change in the center of mass over time and its ascending velocity is shown in Fig. 5, with droplet states at key moments marked on the graph. The overall process can be divided into three stages: (I) droplet growth within the structure (before moment A), (II) droplet bursting and growth out of the structure (moment A to C) and (III) dewetting transitions and jumping stage. At stage I, the condensation droplet grows continuously until it touches the top of micropillars. During stage II, the top of the droplet starts to expand with the wetting contact line pinned at the upper edge of the pillars and the ascending velocity increases steadily. After the contact angle θ_t reaching a critical value, the height of the droplet center of mass again increases at a relatively steady rate with Laplace pressure difference increasing (moment B to C). At stage III, the bottom of the droplet starts to take off from the surface and the liquid column is pressed into the top liquid sphere. The ascending velocity reaches its maximum at moment D and decreases sharply during its detachment from the micropillars. The ability of the droplet to jump depends on whether the kinetic energy of the droplet can overcome the adhesion work exerted on it by the top of pillars. The droplet morphology and vector diagram inside the droplet at different moments are shown in Fig. 6(a). For $t = 0.40$ ms (moment B), as the growth of the droplet top sphere, a small amount of liquid from the bottom is also transported upwards. During stage III, the liquid between the micropillars is pressed into the liquid sphere under the Laplace pressure difference. The maximum local velocity is located at the bottom of the droplet before it detaches from the micropillars, making the adhesion from the top of pillars more significant. The corresponding temperature fields are shown in Fig. 6(b). As the bottom of the droplet breaks away from the surface, the overall temperature gradient inside the droplet decreases.

By adjusting the height of the micropillars and keeping the micropillar spacing constant, the detachment velocities of droplet at different

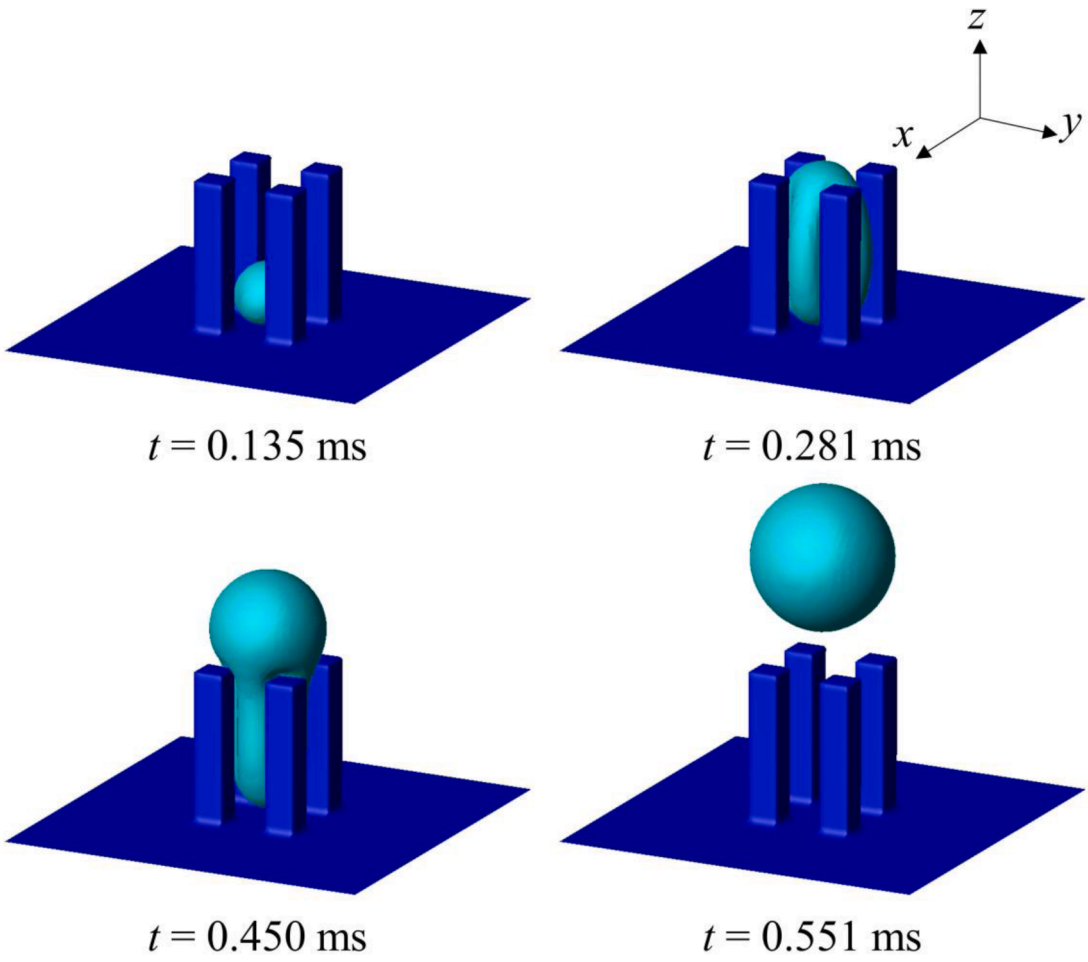

Fig. 4. Single-droplet jumping phenomenon on superhydrophobic microstructured surface during condensation.

aspect ratios ($K = h/l$) are compared (Fig. 7(a)). It should be noted that the maximum velocity represents the ascending velocity of the center of mass before the droplet is completely detached from the structure (e.g. moment D in Fig. 5). When the aspect ratio is equal to 2.0, the droplet cannot overcome the adhesion from the top of micropillars, and eventually only undergoes a state transition without jumping, indicated by a cross in Fig. 7(a). The results show that there is an optimal aspect ratio for the droplet to reach the maximum detaching velocity. And the radius of the liquid sphere at the top when the bottom of the droplet starts to take off from the surface increases slightly with the increase of the aspect ratio.

Energy analysis of droplet detachment and jumping process can be referred to Section S1 in Supporting Information. The analysis process starts when the droplet starts to detach (e.g. moment C in Fig. 5) and ends when the droplet returns to a sphere for the first time (e.g. moment E in Fig. 5). It is observed that condensation can cause the droplet surface area and mass to increase during the detachment process (Figure S1). For the purpose of analysis, the surface area change due to condensation will be rectified by the modified coefficient k_A (see Section S1, Supporting Information). And the mass of the droplet is set to be constant and is taken to be the mass of the droplet when it starts to detach from the surface. To obtain the change in surface area of the droplet, the density at the liquid-vapor interface is defined as $\rho_{lv} = (\rho_l+\rho_v)/2$. The energy conversion efficiency of surface energy to kinetic energy can be calculated as

$$\eta = \frac{E_k}{\Delta E_s} = \frac{0.5 m_0 v_j^2}{\sigma\left[A_0 - (1-k_A)A_j\right]} \tag{17}$$

where E_k is the kinetic energy of the jumping droplet, ΔE_s is the surface energy released by surface area reduction (see Section S1, Supporting Information), m_0 is the mass of the droplet, v_j is the jumping velocity when the droplet returns to a sphere, A_0 is the droplet surface area before detachment, k_A is the surface area variation coefficient and A_j is the surface area of the departing droplet. The energy conversion efficiency for different aspect ratios is shown in Fig. 7(b). When the aspect ratio equals to 3.0, the maximum energy conversion efficiency reaches up to 14.2 %, which is more than twice the energy conversion efficiency for coalescence-induced jumping of binary equally sized droplets [46].

Besides, as the aspect ratio increases, there is a tendency for the lower part of the top liquid sphere to shrink (Fig. 7(d)), which may also be one of the reasons for the pinch-off of the droplet as observed in the experiment [10]. Fig. 7(c) compares the process of droplet condensation on the structured surface with $h = 48\mu m$ at different subcooling degrees by adjusting the wall temperature. With the increase of subcooling, the time required for nucleation of droplet condensation decreases, while the effect of subcooling on droplet ascending velocity is small over the simulated range of subcooling degrees. This is due to the short duration of the detachment process, making it mainly dominated by surface tension and less affected by the condensation rate.

4.3. Directional single-droplet jumping

In order to achieve the directional jumping of droplets, it is easy to think of the design of inclined micropillars. In the following calculations, the structure parameters are set as $a = 12$ μm, $l_1 = 20$ μm, $l_2 = 28$ μm, $h = 50$ μm and the dip angle of the tilted pillars is $\theta = 45°$. The

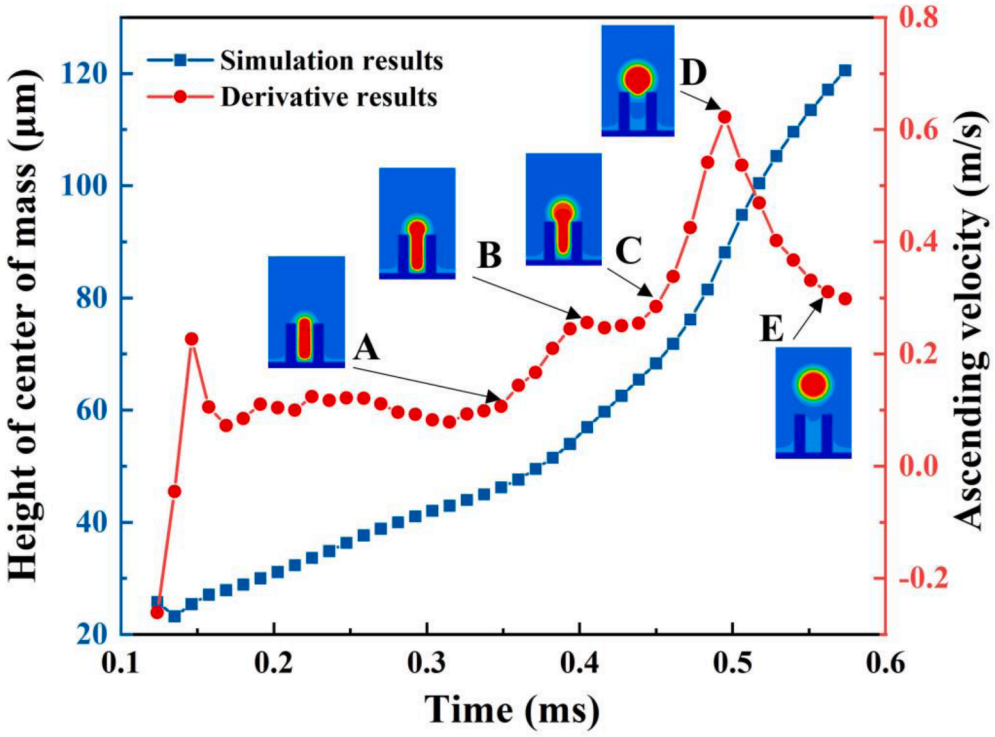

Fig. 5. Variation of the height of center of mass over time and its ascending velocity. The cross sections A~E are intercepted along the diagonal face of the microcolumn to observe the state of the microcolumn and the droplet at the same time.

computational domain is adjusted as 60 × 80 × 140 lattices. The simulation results for such a structure are shown in Fig. 8(a) and self-propelled single droplet jumping is observed. The instantaneous velocity and angle of the droplet center of mass movement are depicted in Fig. 8(a). During stage I, the condensation droplet grows continuously along the micropillars and thus the angle of the droplet center of mass movement maintains at ~45°. After the droplet touches the top of micropillars (stage II), the angle begins to increase as the main portion of the droplet still grows along the micropillars and the upper right side of the droplet starts to expand. During stage III, the top of the droplet bursts from the microstructure in a more vertical direction due to the restriction of the left micropillars (moment B to C). During and after the droplet leaves the structure, the velocity in the z direction decreases more than that in the y direction under the solid-liquid adhesion and gravitational force which results in the decrease of the jumping angle.

The results show that the direction of motion is not completely along the direction of the inclined micropillars as expected. The bursting process during condensation can be described as Fig. 9(a). As the condensate droplet grows, it first touches the tip of the right pillars and starts to burst with the left side still growing along the pillars. Under such an interpretation, if both sides of the droplet can reach the top of the micropillars simultaneously, the droplet direction should be closer to the dip angle of the tilted pillars. On the basis of the original structure, the tips of the four pillars are thus adjusted into the same plane by reducing the height of the left side of the micropillars (Fig. 9(a)). The simulation results of droplet morphology and vector diagram are shown in Fig. 9(b). It can be clearly observed that the kinetic energy of the droplet is transmitted by the liquid column during contraction, and the jumping direction is partially controlled by the top of the micropillars. The evolution of droplet condensation and jumping on the optimized structure is shown in Figure S1 (see supporting information), with the angle between the velocity direction and the horizontal direction ~46.5° at the very moment the droplet detaches from the structure. In conclusion, the direction in which the droplet jumps off the surface depends largely on both the expansion of the top sphere of the droplet and the solid-liquid adhesion. Therefore, in order to control the jumping direction of the droplet, it is also necessary to utilize microstructures to regulate the bursting phase of the droplet, which is often closely related to the top of micropillars.

Based on the above analysis, the more difficult to manufacture inclined micropillars may instead achieve an undesirable result on the directional jumping of droplets. For vertical micropillars, the pressing of the liquid column during condensation is naturally perpendicular to the plane. Therefore, more attention should be paid to the design of the top structure of the pillars for the control of jumping direction. In order to take advantage of droplet bursting process, another structure is shown in Fig. 10, which fixes the height of the micropillars on one side to $h_1 = 48$ μm and increases the height of the micropillars on the other side h_2. The simulation results for $h_2 = 80$μm are displayed in Fig. 10(a), with the change of droplet velocity and jumping angle between the velocity direction and the horizontal direction during stage III shown in Fig. 10(b). For ease of understanding, the droplet can be divided into two parts: the liquid column and the top liquid sphere. During dewetting process, the liquid column moves vertically upward and the top liquid sphere expands to the upper left. By comparing Fig. 10(a) and (b), It can be seen that the angle reaches its minimum value when the liquid column is completely pressed into the top liquid sphere. Now it is clear that the pressing effect of the liquid column on the droplet movement depends on both the direction of the micropillars and the expansion direction of the top droplet, namely the construction of the top of the micropillars. As the liquid column is pressed into the top liquid sphere, the proportion of the liquid column to the total droplet decreases, and the expand direction of the top liquid sphere becomes the main factor affecting the change in the angle of the center of mass movement. During droplet detachment, the angle of the droplet center of mass movement increases again due to the velocity reduction in both the vertical and horizontal directions. By adjusting the height of longer micropillars, the variation of jumping angle with the longer-micropillar height is compared in Fig. 10(c). The unilateral micropillars are increased from 48 to 80 μm and simulated every 8 μm. It can be observed that the growth of the long

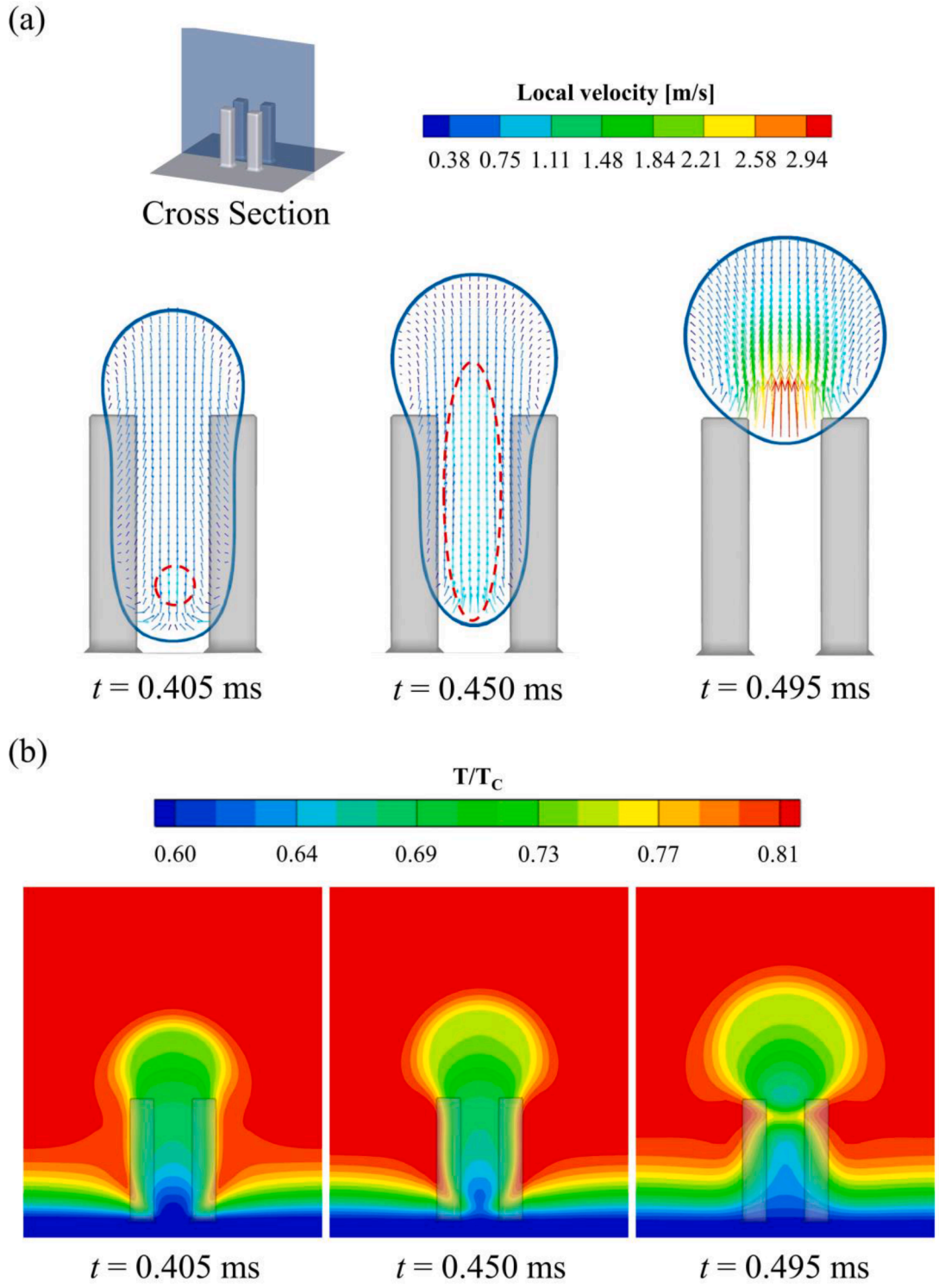

Fig. 6. The evolution of the condensate droplet with time for $h = 56\mu m$, $l_1 = l_2 = 16\mu m$ and $a = 12\mu m$. (a) Droplet morphology and vector diagram at the cross section at different moments. The color of the velocity vector represents the magnitude of the local velocity. (b) The corresponding temperature fields.

pillars strengthens the directional expand of the top liquid sphere and there is an optimal height difference to achieve the most horizontal droplet jumping. To further explain the phenomenon, the change in angle with time was compared for different structures. As shown in Fig. 10(d), the variation of droplet jumping angle with time at different pillar heights can be roughly divided into two stages: (I) expansion dominated stage and (II) horizontal adhesion dominated stage. With the height of the micropillars h_2 increasing, the role of the pillars in guiding the direction during stage (I) becomes obvious and basically reaches its limit after h_2 is taller than 72 μm. On the other hand, the horizontal adhesion keeps increasing with the height of right micropillars during stage II, which causes the angle of the micropillar to decrease when h_2 is taller than 72 μm. The combination of these two factors finally leads to the emergence of the minimum angle.

In order to lessen the effect of the horizontal adhesion from the long pillars (Fig. 10(a)) during droplet detachment, another construction of

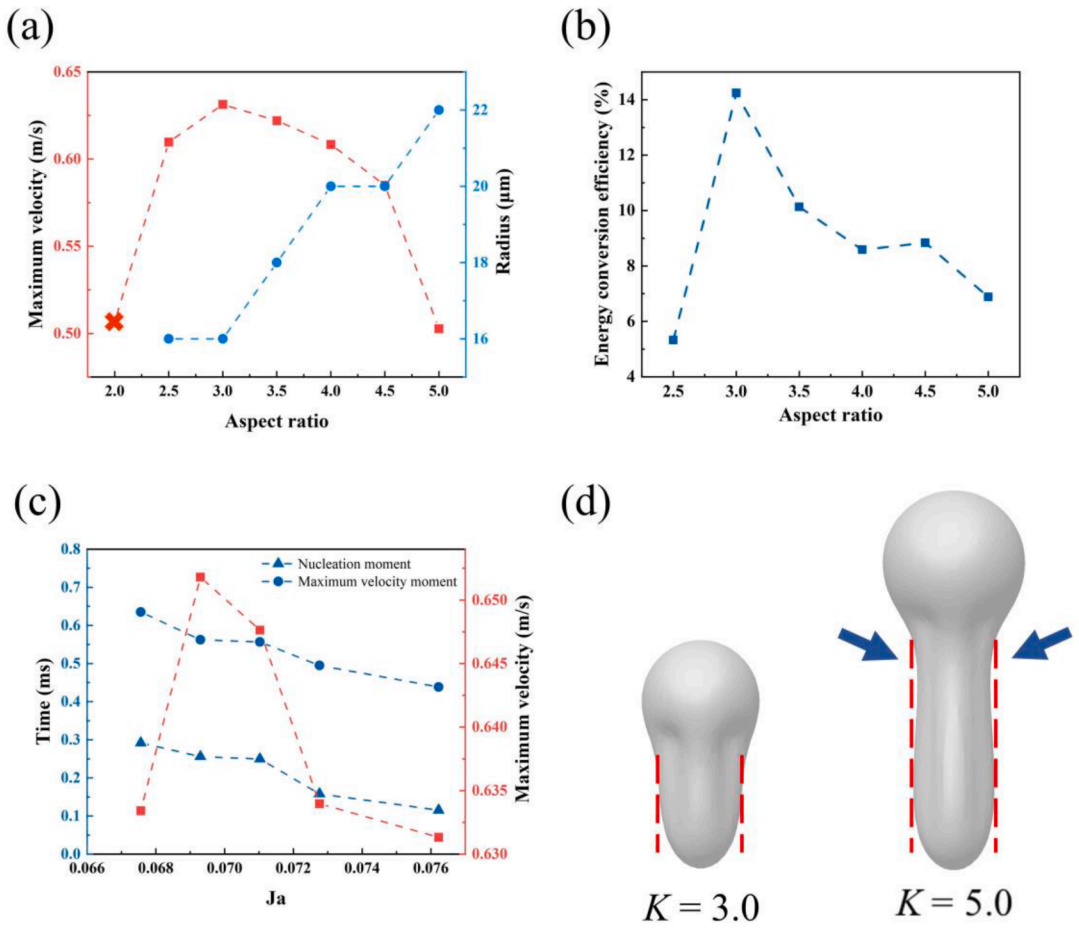

Fig. 7. Effect of surface parameters on droplet condensation and detachment. (a) Comparison of the maximum droplet velocity during condensation under different aspect ratios and the difference of radius of the liquid sphere at the top when the bottom of the droplet starts to take off from the surface. The maximum velocity represents the ascending velocity of the center of mass before the droplet is completely detached from the structure (e.g. moment D in Fig. 5). (b) The energy conversion efficiency for different aspect ratios. (c) Comparison of the nucleation process and droplet jumping during dropwise condensation on the structured surface with $h = 48\mu m$ at different subcooling degrees. (d) Morphological differences of droplets with different aspect ratios.

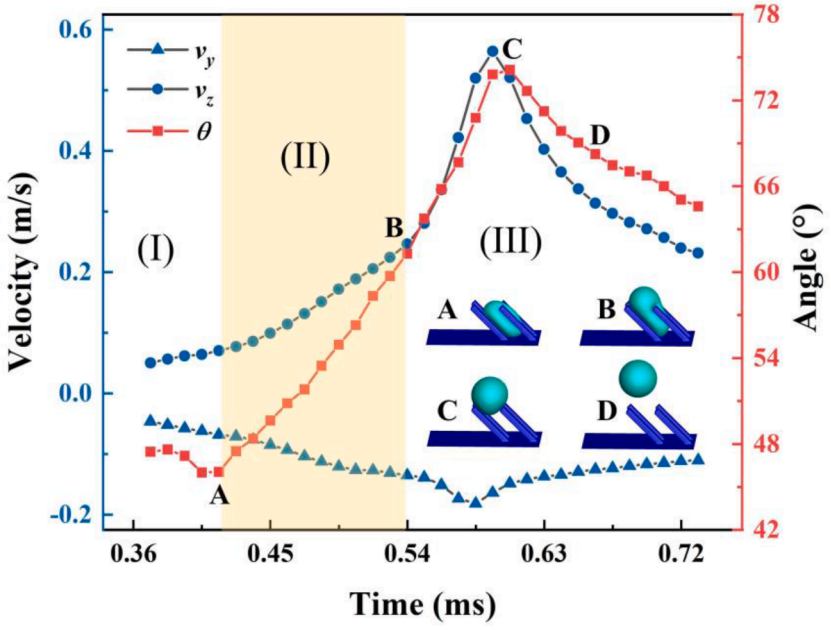

Fig. 8. Self-propelled single droplet jumping from the surface of tilted micropillars whose dip angle $\theta = 45°$.

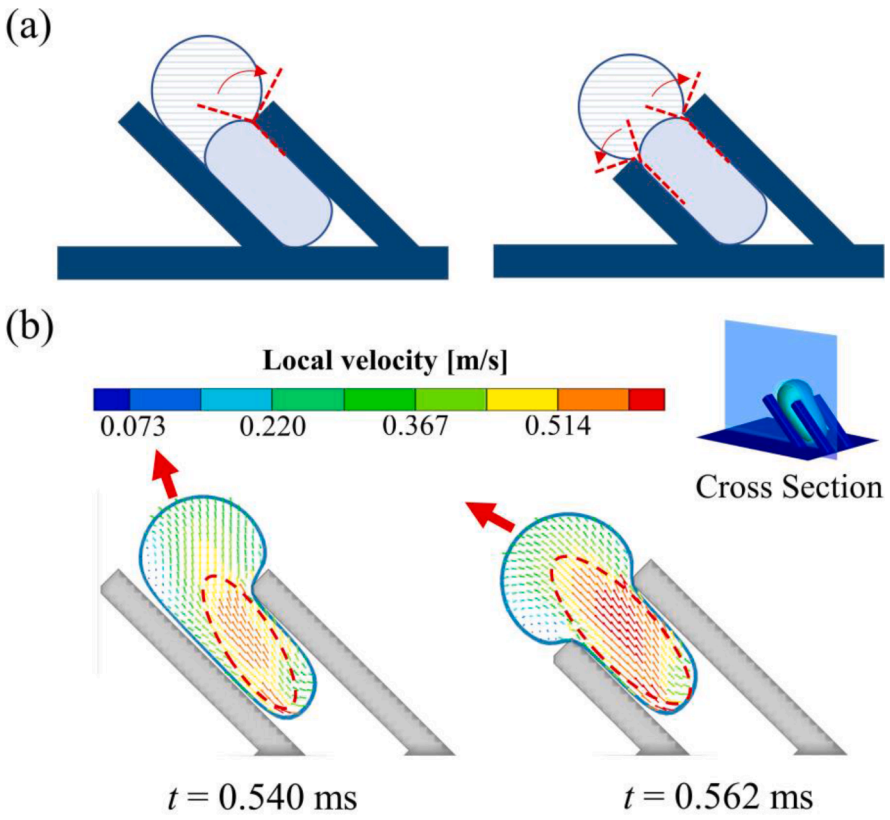

Fig. 9. Droplet morphology on two structures. (a) Schematic diagram of the effect of the top of two structures on the droplet. (b) Droplet morphology and vector diagram at the cross section. The face that is close to the micropillars is selected as the cross-section.

vertical micropillars is carried out as shown in Fig. 11(a). Based on the original structure, the tops of the pillars are beveled at a 45-degree angle with the height of the micropillars maintained. The simulation results for $h = 56\mu m$ are displayed in Fig. 11, which contains the change of droplet velocity and the angle of motion during stage III. As shown in Fig. 11(b), the motion angle of the center of mass decreases during both dewetting process and droplet detachment. In contrast to the last structure, this type does not need to consider the influence of lateral adhesion during droplet detachment. However, the directional jumping of the top-beveled micropillar structure is not obvious at the same time, with the jumping angle between the velocity direction and the horizontal direction ~83° at the very moment the droplet detaches from the structure. Considering the uniform preparation of the structure, the top-beveled micropillar structure is also optional in the case of low directional transport requirements.

4.4. Discussion

In this study, the single droplet morphology during condensation and droplet-structure interaction is analyzed. The mechanism for directional single droplet jumping induced by pinning/stretch and guided by microstructures is explained. Experiments has shown that for the smaller scale groove structures (~10 μm), >90 % of the droplets were removed by self-jumping with no observable coalescence with other droplets [10]. This provides the possibility of applying the single droplet jumping behavior in the reflux of small heat exchangers, such as UTVCs. Therefore, it can be practical to design structures in which single droplet detachment is dominant with other detachment modes supporting in future studies. When single droplet fails to detach from the surfaces, the coalescence-induced jumping will provide certain assist. For example, as shown in Fig. 12, the length, width and height of the fins are set as 12 μm, 68 μm and 48 μm, and the spacing between the fins is set to 16 μm. Compared with micropillars, the groove structure can be more difficult for single droplet to detach from the surface due to the larger solid-liquid contact area. In this case, the role of the combined droplet jumping becomes important.

In addition, as an important physical phenomenon in nature, contact angle hysteresis possesses high research value in the process of single droplet jumping. By adjusting the contact angle hysteresis, the mobility of droplets can be effectively enhanced [47,48]. Therefore, appropriate LBM methods can also be considered to study the influence of contact angle hysteresis on single droplet detachment [49].

5. Conclusion

A three-dimensional non-orthogonal MRT pseudopotential lattice Boltzmann model is adopted to simulate Laplace pressure driven single-droplet jumping on microstructured surfaces during condensation. The effects of subcooling degree and aspect ratio on dropwise condensation and jumping are investigated. Besides, directional single-droplet jumping is observed on the surface of tilted micropillars. The mechanism controlling the directional jumping of droplets is explored by simulations of dropwise condensation on different micropillar surfaces. The conclusions of the study are summarized as follows:

(a) The ascending velocity of the condensate droplet decreases sharply during its detachment from the micropillars. The ability of the droplet to jump mainly depends on whether the kinetic energy of the droplet can overcome the adhesion work exerted on it by the top of pillars.
(b) The droplet only undergoes Wenzel-Cassie state transition without jumping when the aspect ratio is less than 2.0. There exists an optimal aspect ratio for the droplet to reach the maximum detaching velocity. When the aspect ratio equals 3.0, the energy conversion efficiency reaches up to 14.2 %.

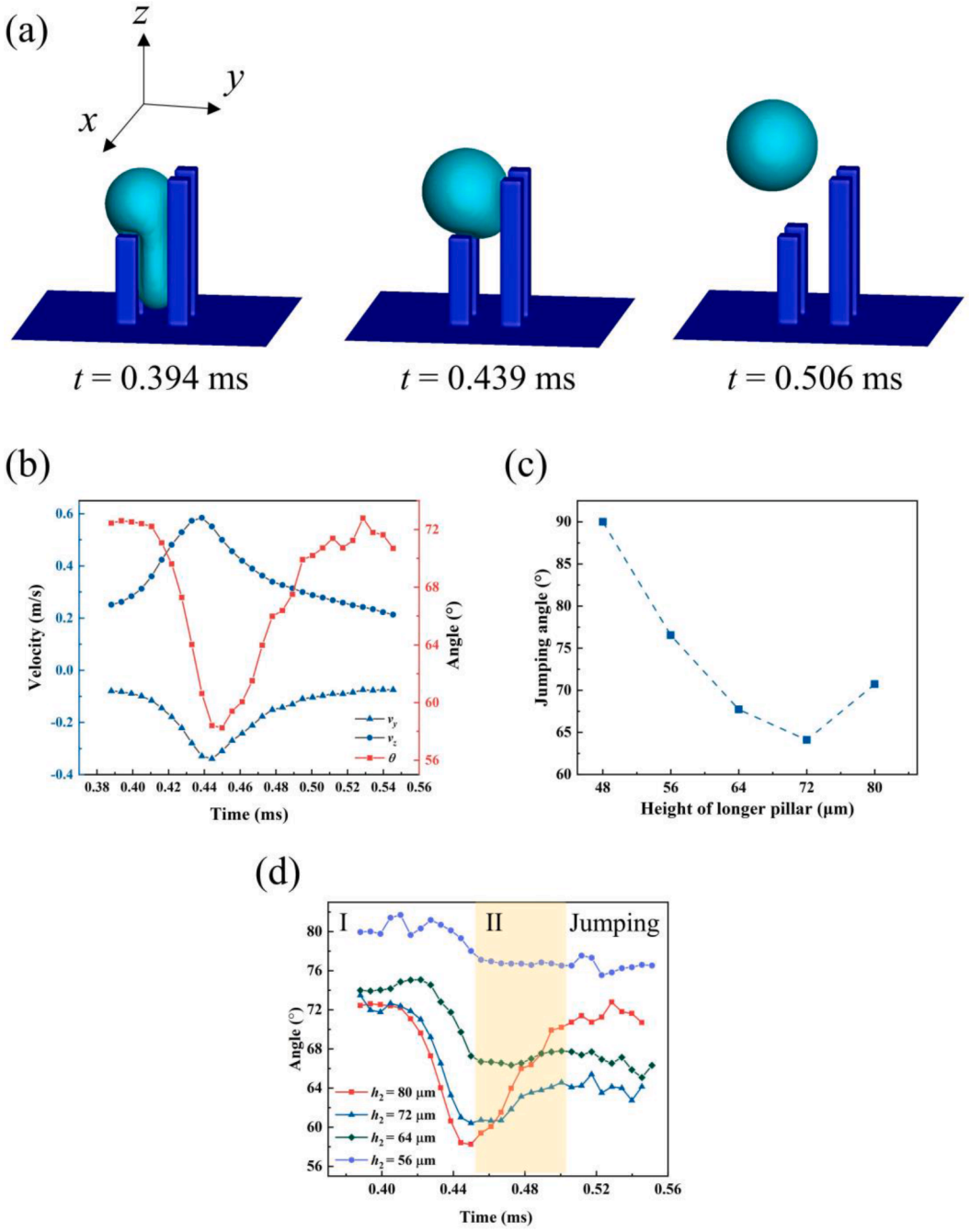

Fig. 10. Simulation results of directional single-droplet jumping during stage III with micropillars of varying length. (a) Morphology of the condensed droplet at different moments; (b) The variation of droplet movement velocity and jumping angle over time; (c) The relationship between jumping angle and the longer-micropillar height; (d) The variation of droplet jumping angle with time at different pillar heights.

Subcooling has less impact on droplet jumping over the simulated range of subcooling degrees.

(c) The direction of droplet jumping is not completely along the direction of the inclined micropillars. The pressing effect of the liquid column makes the droplet movement depend on both the direction of micropillars and the expansion direction of the top liquid sphere, namely the construction of the top of the micropillars. In order to control the jumping direction of the droplet, it is important to utilize microstructures to regulate the bursting phase of the droplet, which is often closely related to the top of micropillars.

(d) For the structure with micropillars of varying length, the growth of the long pillars strengthens the directional expand of the top liquid sphere, with a concomitant increase in horizontal adhesion, pulling the droplets back into the vertical direction.

(e) Compared to the structure with micropillars of varying length, the top-beveled micropillar structure lessens the effect of the horizontal adhesion from the long pillars during droplet detachment. However, the directional expand of the top liquid sphere is not obvious at the same time, resulting in the jumping angle between the velocity direction and the horizontal direction ~83° at the very moment the droplet detaches from the structure.

CRediT authorship contribution statement

Yuhao Zhu: Conceptualization, Investigation, Software, Validation,

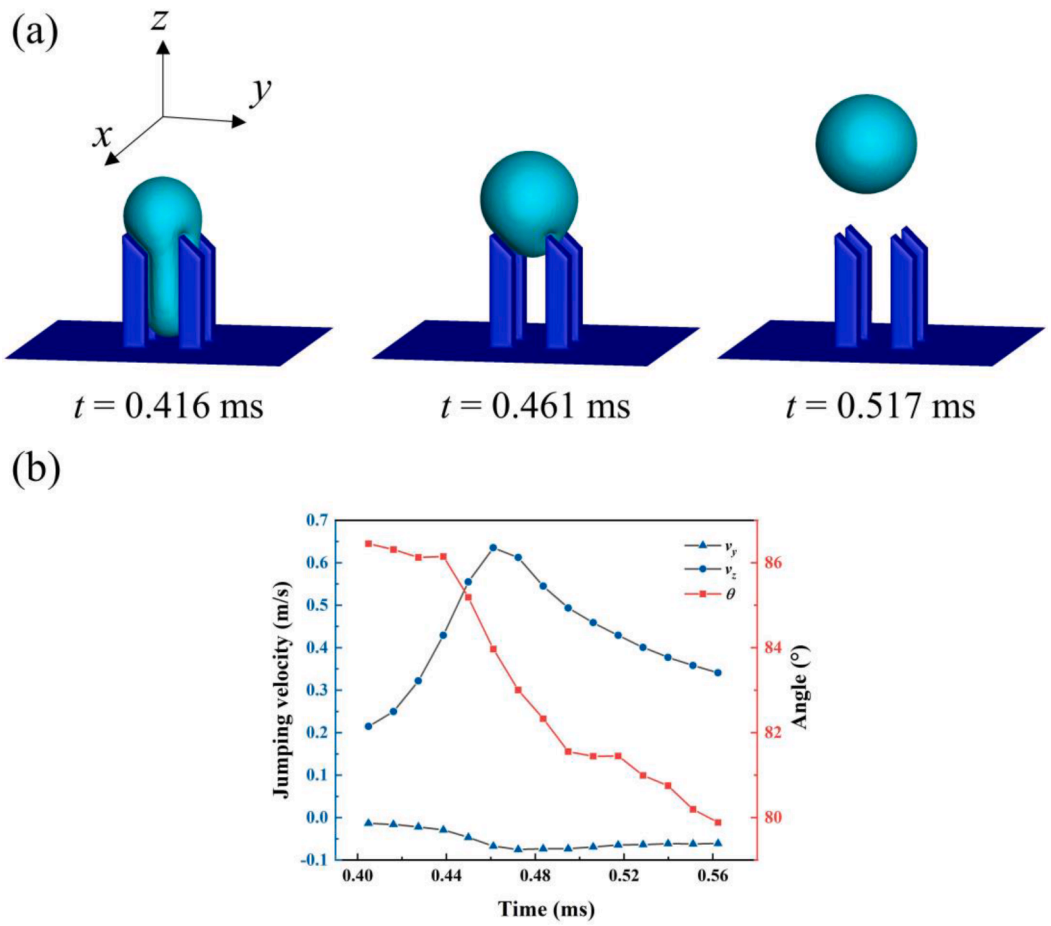

Fig. 11. Simulation results of dropwise condensation on top-beveled micropillar structure during stage III. (a) Morphology of the condensed droplet at different moments; (b) The variation of droplet movement velocity and angle of the center of mass over time.

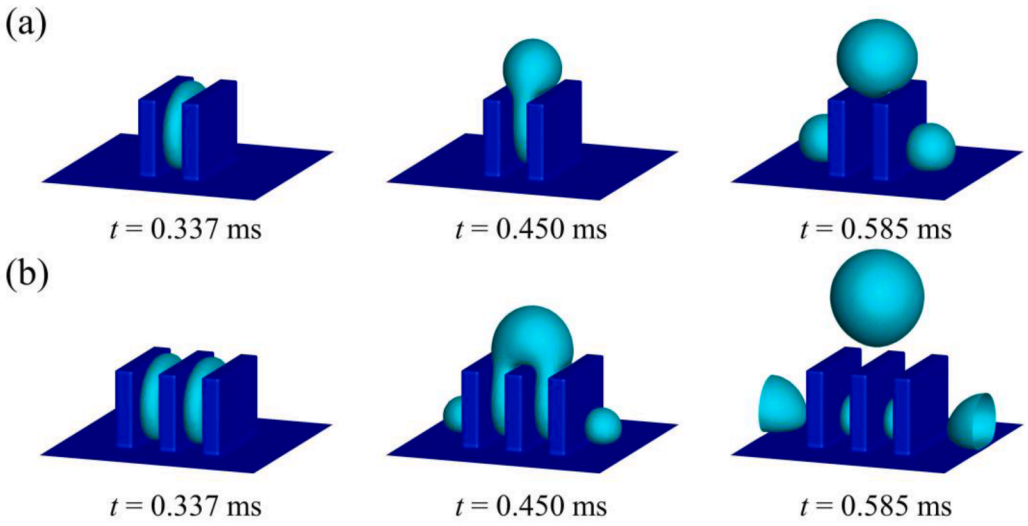

Fig. 12. Simulation results of dropwise condensation on groove-structured surfaces. (a) Single groove structure; (b) Double groove structure.

Writing – original draft. **Shan Gao:** Investigation, Writing – review & editing. **Zhichun Liu:** Funding acquisition, Investigation, Supervision, Writing – review & editing. **Wei Liu:** Investigation, Supervision.

Declaration of competing interest

The authors declare that they have no known competing financial interests or personal relationships that could have appeared to influence the work reported in this paper.

Data availability

Data will be made available on request.

Acknowledgments

This work was supported by the National Natural Science Foundation of China (No. 52076088).

Supplementary materials

Supplementary material associated with this article can be found, in the online version, at doi:10.1016/j.surfin.2024.104055.

References

[1] D. Gurera, B. Bhushan, Designing bioinspired conical surfaces for water collection from condensation, J. Colloid Interface Sci. 560 (2020) 138–148.
[2] D. Song, B. Bhushan, Enhancement of water collection and transport in bioinspired triangular patterns from combined fog and condensation, J. Colloid Interface Sci. 557 (2019) 528–536.
[3] B. Majhy, A.K. Sen, Autonomous droplet transport on a chemically homogenous superhydrophilic surface, Colloid Surf. A-Physicochem. Eng. Asp. 643 (2022) 128798.
[4] G. Zhao, G. Zou, W. Wang, R. Geng, X. Yan, Z. He, L. Liu, X. Zhou, J. Lv, J. Wang, Rationally designed surface microstructural features for enhanced droplet jumping and anti-frosting performance, Soft Matter. 16 (2020) 4462–4476.
[5] N. Miljkovic, R. Enright, Y. Nam, K. Lopez, N. Dou, J. Sack, E.N. Wang, Jumping-Droplet-Enhanced Condensation on Scalable Superhydrophobic Nanostructured Surfaces, Nano Lett. 13 (2013) 179–187.
[6] S.E. Mousavi, A. Moshfegh, H.H. Afrouzi, A. Javadzadegan, D. Toghraie, Simulation of droplet detachment from hydrophobic and hydrophilic solid surfaces under the electric field using Lattice Boltzmann Method (LBM), J. Mol. Liq. 313 (2020) 113528.
[7] S.E. Mousavi Tilehboni, E. Fattahi, H. Hassanzadeh Afrouzi, M. Farhadi, Numerical simulation of droplet detachment from solid walls under gravity force using lattice Boltzmann method, J. Mol. Liq. 212 (2015) 544–556.
[8] X. Wang, J. Chang, Z. Chen, B. Xu, Mesoscopic lattice Boltzmann simulation of droplet jumping condensation heat transfer on the microstructured surface, Int. Commun. Heat Mass Transf. 127 (2021) 105567.
[9] Z. Guo, D. Boylan, L. Shan, X. Dai, Hydrophilic reentrant SLIPS enabled flow separation for rapid water harvesting, Proc. Natl. Acad. Sci. 119 (2022) e2209662119.
[10] X. Yan, Y. Qin, F. Chen, G. Zhao, S. Sett, M.J. Hoque, K.F. Rabbi, X. Zhang, Z. Wang, L. Li, F. Chen, J. Feng, N. Miljkovic, Laplace Pressure Driven Single-Droplet Jumping on Structured Surfaces, ACS Nano 14 (2020) 12796–12809.
[11] D. Gurera, B. Bhushan, Movement of air bubbles under various liquids using bioinspired conical surfaces, J. Colloid Interface Sci. 582 (2021) 41–50.
[12] X. Yan, F. Chen, S. Sett, S. Chavan, H. Li, L. Feng, L. Li, F. Zhao, C. Zhao, Z. Huang, N. Miljkovic, Hierarchical condensation, ACS Nano 13 (2019) 8169–8184.
[13] F. Chu, J. Luo, C. Hao, J. Zhang, X. Wu, D. Wen, Directional transportation of impacting droplets on wettability-controlled surfaces, Langmuir 36 (2020) 5855–5862.
[14] J. Pei, Y. Liao, Q. Li, K. Shi, J. Fu, X. Hu, Z. Huang, L. Xue, X. Xiao, K. Liu, Single-layer graphene prevents Cassie-wetting failure of structured hydrophobic surface for efficient condensation, J. Colloid Interface Sci. 615 (2022) 302–308.
[15] C. Lv, P. Hao, X. Zhang, F. He, Dewetting transitions of dropwise condensation on nanotexture-enhanced superhydrophobic surfaces, ACS Nano 9 (2015) 12311–12319.
[16] A. Aili, H. Li, M.H. Alhosani, T. Zhang, Unidirectional fast growth and forced jumping of stretched droplets on nanostructured microporous surfaces, ACS Appl. Mater. Interfaces 8 (2016) 21776–21786.
[17] Q. Peng, X. Yan, J. Li, L. Li, H. Cha, Y. Ding, C. Dang, L. Jia, N. Miljkovic, Breaking droplet jumping energy conversion limits with superhydrophobic microgrooves, Langmuir 36 (2020) 9510–9522.
[18] F. Zhou, J. Zhou, X. Huai, Advancements and challenges in ultra-thin vapor chambers for high-efficiency electronic thermal management: a comprehensive review, Int. J. Heat Mass Transf. 214 (2023) 124453.
[19] C. Wei, Y. Zong, Y. Jiang, Bioinspired wire-on-pillar magneto-responsive superhydrophobic arrays, ACS Appl. Mater. Interfaces 15 (2023) 24989–24998.
[20] C.R. Kharangate, I. Mudawar, Review of computational studies on boiling and condensation, Int. J. Heat Mass Transf. 108 (2017) 1164–1196.
[21] X. Wang, B. Xu, Z. Chen, Y. Yang, Q. Cao, Lattice Boltzmann simulation of dropwise condensation on the microstructured surfaces with different wettability and morphologies, Int. J. Therm. Sci. 160 (2021) 106643.
[22] Z. Xu, J. Li, Z. Yao, J. Li, Effects of superheat degree and wettability on droplet evaporation time near Leidenfrost point through Lattice Boltzmann simulation, Int. J. Therm. Sci. 167 (2021) 107017.
[23] C. Xie, J. Zhang, V. Bertola, M. Wang, Droplet evaporation on a horizontal substrate under gravity field by mesoscopic modeling, J. Colloid Interface Sci. 463 (2016) 317–323.
[24] X. Shan, H. Chen, Lattice Boltzmann model for simulating flows with multiple phases and components, Phys. Rev. E 47 (1993) 1815–1819.
[25] S. Mukherjee, J. Abraham, A pressure-evolution-based multi-relaxation-time high-density-ratio two-phase lattice-Boltzmann model, Comput. Fluids 36 (2007) 1149–1158.
[26] S. Gong, P. Cheng, A lattice Boltzmann method for simulation of liquid–vapor phase-change heat transfer, Int. J. Heat Mass Transf. 55 (2012) 4923–4927.
[27] Q. Li, K.H. Luo, X.J. Li, Lattice Boltzmann modeling of multiphase flows at large density ratio with an improved pseudopotential model, Phys. Rev. E 87 (2013) 053301.
[28] A. Ashrafi-Habibabadi, A. Moosavi, Droplet condensation and jumping on structured superhydrophobic surfaces, Int. J. Heat Mass Transf. 134 (2019) 680–693.
[29] M. Li, C. Huber, W. Tao, J. Wei, Study on nucleation position and wetting state for dropwise condensation on rough structures with different wettability using multiphase lattice Boltzmann method, Int. J. Heat Mass Transf. 131 (2019) 96–100.
[30] H. Zhou, Z. Xu, D. Li, Y. Shang, P. Yuan, Lattice Boltzmann simulation of droplet impact dynamics on superhydrophobic surface decorated with triangular ridges, Colloid Surf. A-Physicochem. Eng. Asp. 654 (2022) 130204.
[31] S. Farokhirad, T. Lee, Computational study of microparticle effect on self-propelled jumping of droplets from superhydrophobic substrates, Int. J. Multiphase Flow 95 (2017) 220–234.
[32] X. Liu, P. Cheng, 3D multiphase lattice Boltzmann simulations for morphological effects on self-propelled jumping of droplets on textured superhydrophobic surfaces, Int. Commun. Heat Mass Transf. 64 (2015) 7–13.
[33] X. Liu, P. Cheng, X. Quan, Lattice Boltzmann simulations for self-propelled jumping of droplets after coalescence on a superhydrophobic surface, Int. J. Heat Mass Transf. 73 (2014) 195–200.
[34] S.-F. Zheng, U. Gross, X.-D. Wang, Dropwise condensation: from fundamentals of wetting, nucleation, and droplet mobility to performance improvement by advanced functional surfaces, Adv. Colloid Interface Sci. 295 (2021) 102503.
[35] Q. Li, D.H. Du, L.L. Fei, K.H. Luo, Three-dimensional non-orthogonal MRT pseudopotential lattice Boltzmann model for multiphase flows, Comput. Fluids 186 (2019) 128–140.
[36] P. Zhou, W. Liu, Z. Liu, Lattice Boltzmann simulation of nucleate boiling in micro-pillar structured surface, Int. J. Heat Mass Transf. 131 (2019) 1–10.
[37] S. Gong, P. Cheng, Numerical investigation of droplet motion and coalescence by an improved lattice Boltzmann model for phase transitions and multiphase flows, Comput. Fluids 53 (2012) 93–104.
[38] P. Yuan, L. Schaefer, Equations of state in a lattice Boltzmann model, Phys. Fluids 18 (2006) 042101.
[39] S. Gong, P. Cheng, Direct numerical simulations of pool boiling curves including heater's thermal responses and the effect of vapor phase's thermal conductivity, Int. Commun. Heat Mass Transf. 87 (2017) 61–71.
[40] G. Hazi, A. Markus, On the bubble departure diameter and release frequency based on numerical simulation results, Int. J. Heat Mass Transf. 52 (2009) 1472–1480.
[41] A. Ashrafi, A. Moosavi, Droplet condensation on chemically homogeneous and heterogeneous surfaces, J. Appl. Phys. 120 (2016).
[42] I.O. Ucar, H.Y. Erbil, Dropwise condensation rate of water breath figures on polymer surfaces having similar surface free energies, Appl. Surf. Sci. 259 (2012) 515–523.
[43] A.J.C. Ladd, Numerical simulations of particulate suspensions via a discretized Boltzmann equation. Part 1. Theoretical foundation, J. Fluid Mech. 271 (1994) 285–309.
[44] Q. Zou, X. He, On pressure and velocity boundary conditions for the lattice Boltzmann BGK model, Phys. Fluids 9 (1997) 1591–1598.
[45] X. Liu, P. Cheng, Lattice Boltzmann simulation of steady laminar film condensation on a vertical hydrophilic subcooled flat plate, Int. J. Heat Mass Transf. 62 (2013) 507–514.
[46] X. Yan, L. Zhang, S. Sett, L. Feng, C. Zhao, Z. Huang, H. Vahabi, A.K. Kota, F. Chen, N. Miljkovic, Droplet Jumping: effects of Droplet Size, Surface Structure, Pinning, and Liquid Properties, ACS Nano 13 (2019) 1309–1323.
[47] X. Dai, B.B. Stogin, S. Yang, T.-S. Wong, Slippery Wenzel State, ACS Nano 9 (2015) 9260–9267.
[48] L. Zhang, Z. Guo, J. Sarma, W. Zhao, X. Dai, Gradient quasi-liquid surface enabled self-propulsion of highly wetting liquids, 31 (2021) 2008614.
[49] H. Liu, Y. Ju, N. Wang, G. Xi, Y. Zhang, Lattice Boltzmann modeling of contact angle and its hysteresis in two-phase flow with large viscosity difference, Phys. Rev. E 92 (2015) 033306.